Optical-Resonance-Enhanced Photoemission from Nanostructured GaAs Photocathodes

Xincun Peng,[1,2,*] Zhidong Wang,[1] Yun Liu,[1] Dennis M. Manos,[3] Matt Poelker,[2] Marcy Stutzman,[2] Bin Tang,[1] Shukui Zhang,[2,†] and Jijun Zou[1,2,3,‡]

[1] *Engineering Research Center of New Energy Technology of Jiangxi Province, East China University of Technology, Nanchang, 330013, China*

[2] *Thomas Jefferson National Accelerator facility, 12000 Jefferson Avenue, Newport News, Virginia, 23606, USA*

[3] *William and Mary, Williamsburg, Virginia, 23185, USA*

(Received 10 July 2019; revised manuscript received 15 July 2019; published 2 December 2019)

A negative electron affinity photocathode based on GaAs nanopillar-array (NPA) Mie-type resonators is demonstrated and significant quantum efficiency enhancement is observed. Nanophotonic resonance-assisted photoelectron emission into vacuum is investigated, indicating an enhanced density of optical states due to increased light concentration and increased electron emission area. For visible wavelengths, the Mie resonances in GaAs NPA reduce light reflectivity to less than 6% compared to a typical value >35% and result in maximum quantum efficiency 3.5 times greater than a GaAs wafer photocathode without the NPA structure. Comprehensive simulations and experimental studies are presented.

DOI: 10.1103/PhysRevApplied.12.064002

I. INTRODUCTION

Optical resonance can be excited by the interaction between free-space propagating light and subwavelength nanostructured materials, which has been shown to be highly effective for light management in optoelectronic devices [1,2]. Recently, semiconductor subwavelength nanostructures formed in materials with high indices of refraction have attracted increased attention because of their ability to support geometrical resonances (Mie-type, plane-wave scattering from spheres, cylinders, or other shapes) with very low-parasitic-power absorption loss and for their compatibility with semiconductor device processing [3]. In this study, we investigate Mie-type nanostructured resonators to enhance the photoelectron emission properties of semiconductor photocathodes, which we believe could foster alternative opportunities for generating high quality electron beams using negative electron affinity (NEA) GaAs or similar semiconductor-based photocathodes [4] for large-scale electron accelerators [5,6], advanced light sources [7,8], high-resolution spectral low-light-level imaging [9,10], low-energy electron microscopes [11] and electron beam lithography [12]. Some of these applications require photocathodes that provide high electron spin polarization, ESP, but with photoelectron emission quantum efficiency, QE, higher than is available today [4–8]. The highest ESP reported to date (92%) was obtained using strained superlattice NEA photocathodes [13]. However, these photocathodes cannot meet the increasing demands for both reasonable lifetime and high QE for proposed next-generation large-scale electron accelerator facilities, where both high brightness and high-average-current-polarized electron beams are required [14]. Photocathodes with low QE would require excessive laser power to generate the desired high current electron beams, and photocathode heating due to the laser power deposited into the cathode substrate leads to QE decay and unacceptably short operational lifetime [15,16]. Some alternative GaAs-based thin film structures [17–20] have been explored to improve QE, however, the performance of these film-structured devices has been limited by the mismatch between the carrier diffusion length and optical absorption depth [21]. In addition, the high index of refraction of GaAs causes up to 35% of the incident light to be reflected from the surface. Scattered laser light at the edge of the photocathode can generate unwanted electron emission that strikes the vacuum chamber walls degrading the vacuum and reducing photogun operating lifetime [22].

A Mie resonator is a nanostructured device that confines and concentrates the incident light in a well-defined spatial mode profile inside the nanostructure by exciting both electric and magnetic dipoles and higher-order multipole resonances. A strong Mie resonance effect is often excited in materials with a high index of refraction [1]. In the visible spectral range, recent work has focused

*pengxincun@yahoo.com
†shukui@jlab.org
‡jjzou@ecit.cn

on Si semiconductor nanoresonators with large scattering cross sections, to couple and confine light in optoelectronic applications [23–25]. Compared to the low visible-light absorptivity associated with the indirect band gap of Si, nanoresonators in direct bandgap GaAs promise much higher natural absorption. Also, in nanostructured GaAs, the process of light absorption can be decoupled from carrier collection by strong light concentration [26,27]. This has been demonstrated in GaAs nanowire resonator solar cells, where light absorption enhancement has been increased by a factor of approximately 70 with respect to flat films, yielding efficiencies beyond the Shockley-Queisser limit [27]. But despite this exciting result and others [27,28], it remains difficult to fabricate *p-n* junctions and electrodes of typical diode-type devices such as solar cells using nanoscaled resonators. In contrast, for a NEA photocathode, where the required bias can be applied externally and only *p*-doped GaAs is needed [9,15], the fabrication process is much simpler.

We report the demonstration of a NEA photocathode based on nanostructured GaAs in which a *p*-doped GaAs nanopillar-array (NPA) resonator is set as the primary device function region to enhance the photoelectron emission into vacuum. GaAs NPAs are fabricated by Substrate-Conformal Imprint Lithography (SCIL) [29], and the surface is activated to the NEA state to measure the photoelectron emission QE in an ultrahigh vacuum (UHV) test apparatus. The Mie-type electric magnetic dipoles and quadrupole resonance modes are demonstrated in NPAs and the surface reflectance can be significantly reduced to less than 6% at the resonance wavelengths. Compared with the flat wafer, QE enhancement by a factor of 3.5 is achieved in NPAs at the resonance wavelength. This optically "dark" photocathode (low light reflectance) but possessing electrically "high brightness" (enhanced electron emission) provides alternative opportunities for practical applications such as large-scale electron accelerators and high-resolution spectral low-light-level imaging.

II. DEVICE STRUCTURE AND METHODS

The nanostructured photocathode under investigation is composed of a hexagonal nanopillar-array (NPA) fabricated on a *p*-doped (concentration $N_A = 10^{19}$ cm^{-3}) GaAs substrate that can be activated to a NEA state by coadsorption of Cs and F [15,19], as shown in Fig. 1(a). The dimensions of the structure include the period of the hexagonal lattice *P*, the pillar diameter *D,* and height *H*. Figure 1(b) depicts the fabrication process of this structure. A Si hexagonal NPA master pattern fabricated by electron beam lithography (EBL) and reactive ion etching (RIE) is first duplicated by fabricating a flexible polydimethysiloxane (PDMS) nanohole array stamp. For the GaAs wafer, the first step is to deposit a layer of silicon dioxide (SiO_2) onto a GaAs (100) substrate using plasma-enhanced chemical vapor deposition (PECVD). A layer of poly(methyl methacrylate) (PMMA) photoresist layer is spin coated onto the SiO_2 layer, then the flexible PDMS stamp is applied using a dedicated SCIL imprint mechanical tool. The sample then undergoes RIE (Tegal 903e) to transfer the pattern to the SiO_2 hard mask. Finally, an optimized inductively coupled plasma etch (ICP, Oxford Plasmalab System 100 ICP180) is used to obtain the GaAs NPA. The PMMA is removed with acetone, and the SiO_2 mask layer is then removed with buffered oxide etchant, leaving only the GaAs NPAs on the substrate. The morphology of the GaAs NPA is imaged with a field emission scanning electron microscope (SEM, NOVA NANOSEM 450). Reflectance spectra are measured using a spectrometer (NOVA-EX, Ideaoptics Instruments, China) at 0° incident angle.

The GaAs NPA samples are installed in an UHV chamber with a base pressure of approximately 10^{-11}Torr [See Fig. 1(c)]. The chamber is baked in a thermally insulated enclosure at 200 °C for over 30 h to remove water vapor. Following the bake and cool down to room temperature, the sample is heated to approximately 540 °C, cooled to room temperature, and then activated to reach the NEA condition using the standard "yo-yo" activation procedure with cesium and NF3 [9,15]. A tunable supercontinuum light source (NKT Photonics) provides μW of well-collimated light with the wavelengths, λ, from 400 to 850 nm and a picoammeter (Keithley 485) is used to measure the photoelectron emission from the GaAs NPA photocathode for the QE measurements. Figure 1(d) shows the time dependence of the electron current during the typical "yo-yo" NEA activation for a GaAs NPA photocathode.

The photoemission process of the NEA photocathode can be described using Spicer's three-step model [30] comprised of photoelectron excitation, electron transportation to surface, and escape into vacuum, as illustrated in Fig. 2(a). These steps are also illustrated in Fig. 2(b) for a NPA photocathode to compare to a flat-surface GaAs referred to hereafter as a flat wafer photocathode, in Fig. 2(c). From Figs. 2(b) and 2(c), we can see the advantages of NPA. First, light absorption in NPA is much larger than that in a flat wafer because the local density of optical states (LDOS) in nanopillars can be enhanced by Mie resonance [25]. The photoelectrons can be highly localized inside nanopillar resonators near the top and side surfaces [26] where electrons can be efficiently transported and emitted into vacuum due to the much lower transportation distance than that of the flat wafer, which leads to enhanced QE. Furthermore, a NPA photocathode has a larger effective electron emission area (a_{NPA}) compared to a flat wafer (a_{flat}) due to the fact that both the top and side surfaces of the nanopillar can be activated to the NEA state, which also permits a larger QE. For the hexagonal NPA, the ratio

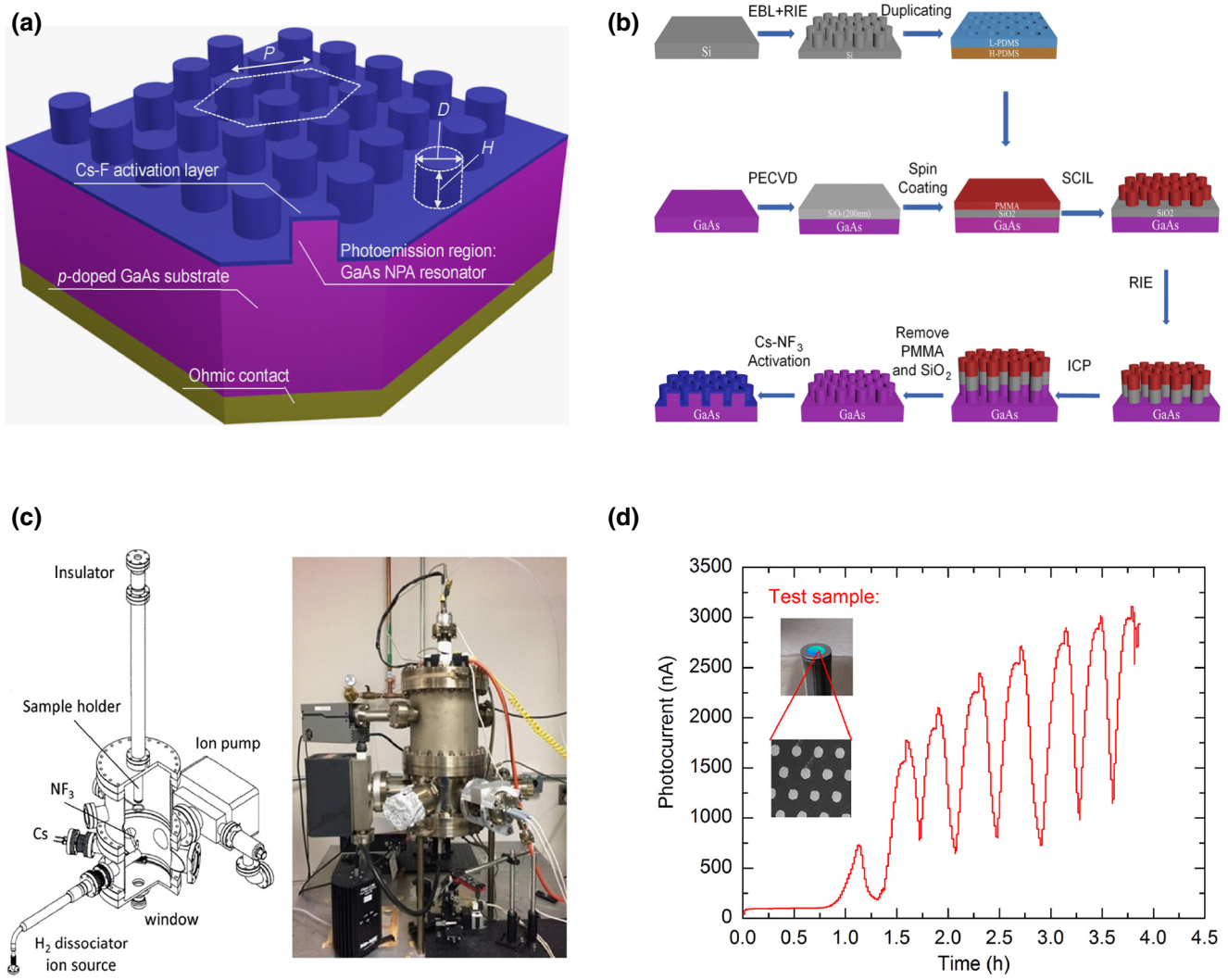

FIG. 1. Hexagonal GaAs NPA resonator photocathode. (a) Device structure. (b) Schematics of the fabrication process. (c) Ultrahigh vacuum chamber used for the NEA activation and QE measurement. (d) Time evolution of photocurrent during a typical "yo-yo" activation for a GaAs NPA photocathode together with a photograph of one sample mounted to a holder for installation in the ultrahigh vacuum test chamber.

of a_{NPA} to a_{flat}, r_{emi}, provides a measure of the emission area enhancement and can be calculated by

$$r_{\mathrm{emi}} = 1 + (2\pi DH)/(\sqrt{3}P^2). \tag{1}$$

The low transportation distance in nanopillars also permits the high transportation efficiency of the electrons in higher L and X valleys of the GaAs conduction band beside the lowest Γ valley, as shown in Fig. 2(a). S. Karkare, *et al.*, have reported that the X valley holds up only to incident photon energy of 2.4 eV [5]. In this work, we investigate the NPA photocathodes with the Mie resonance within the wavelength range of 600–700 nm (photon energy of 1.8–2 eV), so the two-valley (Γ and L) diffusion model [31] is used to analyze the transportation properties. The three-dimensional fully coupled electron diffusion equations for the Γ and L valleys are [31]

$$D_\Gamma \nabla^2 n_\Gamma(\lambda,x,y,z) - \frac{n_\Gamma(\lambda,x,y,z)}{\tau_{\Gamma V}} + \frac{n_\Gamma(\lambda,x,y,z)}{\tau_{L\Gamma}} + g(\lambda,x,y,z)F_\Gamma(\lambda) = 0, \tag{2}$$

$$D_{\mathrm{L}} \nabla^2 n_L(\lambda,x,y,z) - \frac{n_L(\lambda,x,y,z)}{\tau_{L\Gamma}} + g(\lambda,x,y,z)F_L(\lambda) = 0, \tag{3}$$

where F_Γ/F_L, $\tau_{\Gamma V}/\tau_{L\Gamma}$, and D_Γ/D_L are the fraction of the photoexcited electrons and the lifetime and diffusion coefficients of electrons in the Γ and L valleys, respectively. These intrinsic material parameters are taken from other reported results for the GaAs wafer photocathodes

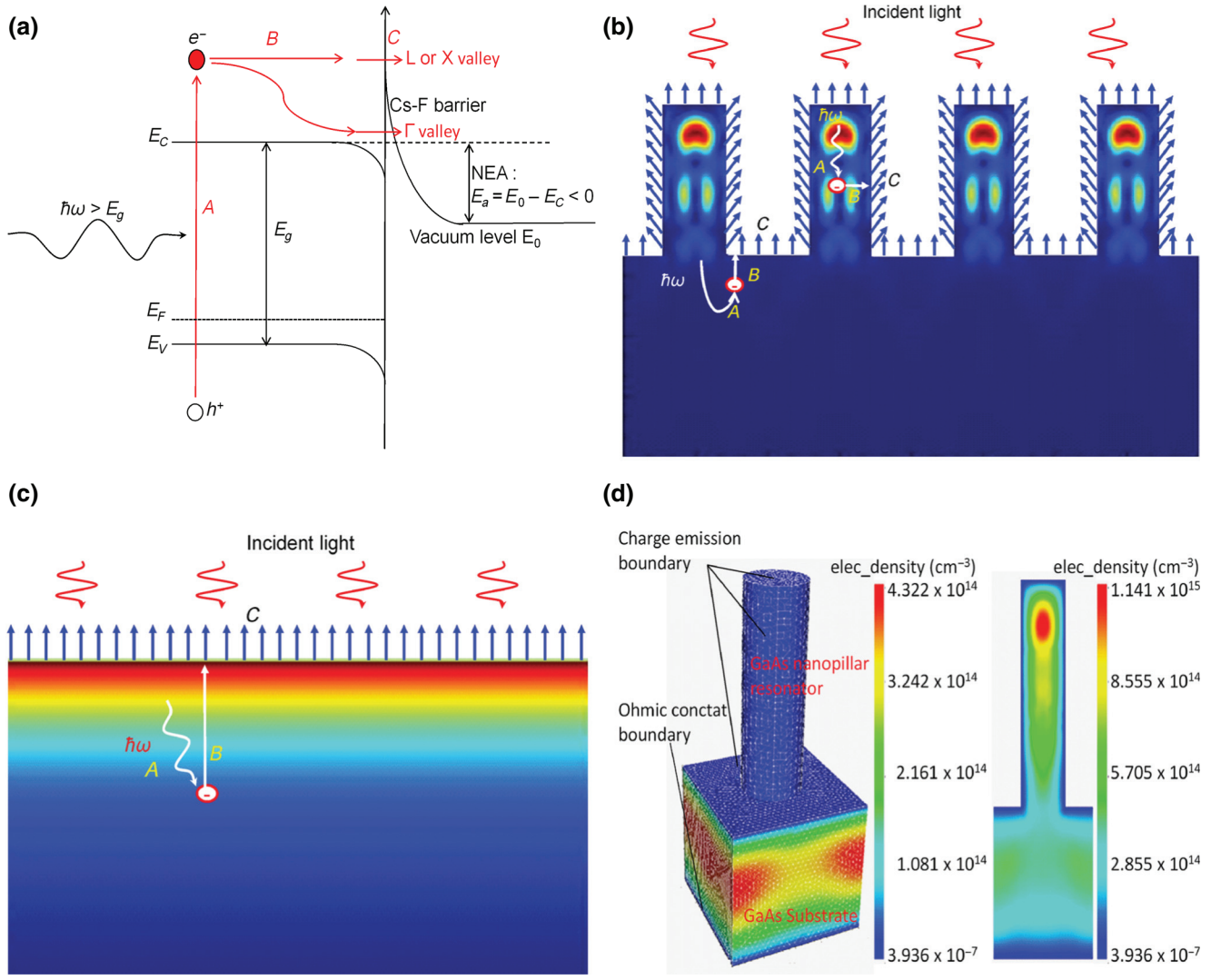

FIG. 2. Photoemission model of the GaAs NPA resonator photocathode. (a) The electronic band structure and photoemission process of the NEA photocathode based on Spicer's model, with letters *A*, *B*, and *C* signifying the processes of photoelectron excitation, electron transportation to surface, and escape from the surface into vacuum, respectively. (c) and (d) are the photoemission processes of GaAs NPA and flat wafer photocathodes, respectively. The red color regions denote areas where light absorption is greatest and the blue arrows indicate the trajectories of photoemitted electrons. (d) TCAD setup for analyzing the photoelectric properties of the GaAs NPA photocathode, with the electron density distributions [elec._density (cm^{-3})] on the three-dimensional surfaces (left) and on the vertical center cross section (i.e., the cross-section plane that contains the pillar axis of symmetry) of GaAs NPA are illustrated (right), respectively. Note the two color bars are independent and not scalable to each other.

[31–33]. g (λ, x, y, z) is the spatial distribution of the photogeneration rate of the electron-hole pairs, which is equivalent to the light absorption rate for GaAs at the visible waveband and can be calculated by the finite difference time domain (FDTD, Lumerical FDTD Solutions [34]) method. n_Γ (λ, x, y, z) and n_L (λ, x, y, z) are the spatial distributions of electron concentrations in the Γ and *L* valleys, respectively.

The n_Γ and n_L in Eqs. (2) and (3) are solved by a full Newton's scheme using a Cogenda visual TCAD tool [35]. Figure 2(d) shows the TCAD setup in which the bottom and top surfaces are set as an Ohmic contact and charge emission boundary conditions, respectively. Figure 2(d) also shows the electron density distributions, which are determined by photon absorption, electron diffusion, and surface boundary conditions. Under the above boundary conditions, all of the electrons reaching the cathode surfaces will be collected either through emission (for charge emission) or recombination (for both charge emission and Ohmic contact), and the electron density should be very low or ideally 0 at the surface boundary. The electron current densities emitted into vacuum for the Γ (J_Γ) and

L (J_L) valleys are then given by

$$J_\Gamma(\lambda) = qP_\Gamma D_\Gamma \nabla n_\Gamma(\lambda, x, y, z)|_{\text{surface}}, \quad (4)$$

$$J_L(\lambda) = qP_L D_L \nabla n_L(\lambda, x, y, z)|_{\text{surface}}, \quad (5)$$

where q is the elementary charge. P_L and P_Γ are the escape probabilities of electrons emitted into vacuum from the L and Γ valleys, respectively. P_L and P_Γ are determined by the surface NEA state that has a very strong dependence on the surface cleanliness, vacuum conditions, and the details of the activation procedure. This varies from sample to sample and from activation to activation and is difficult to reproduce exactly in experiment. In this work, P_L and P_Γ are obtained by fitting the theoretical model to the measured QE from the test samples. Our previous reports have demonstrated that a constant P_L and a P_Γ (λ) exponentially related to wavelength can give good fitting results [32,33]. P_Γ (λ) is written as [32]

$$P_\Gamma(\lambda) = P_\Gamma \exp[k(1/1.42 - \lambda/1.24)], \quad (6)$$

where k is a coefficient, which we call the surface potential barrier factor. The fitting parameters are P_L, P_Γ, and k.

Assuming $\Phi(\lambda)$ is the incident photon flux density as a function of λ, the quantum efficiency QE (λ) of a GaAs NEA photocathode will be

$$\text{QE}(\lambda) = \left| \frac{(J_\Gamma(\lambda) + J_L(\lambda))}{q\Phi(\lambda)} \right| \times 100\%. \quad (7)$$

III. RESULTS AND DISCUSSION

A. Mie-resonance-enhanced light absorption in GaAs NPA

To understand the resonance-enhanced light absorption in NPA, the FDTD method is used to model the light absorption, η_a, of the nanopillars in the GaAs NPA as a function of its geometric parameters and the light wavelength, λ, of the plane-wave radiation propagating along the nanopillar axes. Figure 3(a) shows the dependence of η_a on λ and D for the hexagonal GaAs NPA with $H = 750$ nm and $P = 600$ nm. The NPA filling fraction, f, which is defined as the rate of the projected physical area for the nanopillar to that for the whole device surface, is also shown in Figs. 3(a) and 3(d). Some dominant absorption spectra branches are notably present, corresponding to the Mie resonances similar to those reported using nanostructures of Si [25]. These branches can be explained with Mie's theory [1], namely, the first-order magnetic electric dipole (MD-ED) resonance mode is excited when $(Dn)/\lambda = 1$ with n being the refractive index, whereas the quadrupole (MQ-EQ), and higher-order multipole modes, are excited for larger values of $(Dn)/\lambda$, which are labeled at the corresponding η_a peaks in Fig. 3(a). Figure 3(b) gives the normalized electric magnetic profiles (|E|-|H|) and field lines of dipole [black dot $M1$ in Fig. 3(a)] and quadrupole [black dot $M2$ in Fig. 3(a)] modes, which could be used to determine the Mie-resonance modes, which are consist with the results reported for others such as Si [25]. Both the dipole and quadrupole resonance-dominated η_a peak wavelengths change with D across the 500–850 nm waveband, consistent with photoemission requirements of GaAs NEA photocathodes.

It can be seen from Fig. 3(a) that the values of the resonance-enhanced η_a appears to be fairly constant and only changes slightly as D changes, but is quite sensitive to H and P as shown in Figs. 3(c) and 3(d), which presents the simulated results for the dipole mode NPA resonators with $D = 120$ nm at $\lambda \sim 620$ nm. Larger pillar height leads to stronger resonance electromagnetic field coupling in nanopillars and provides stronger absorption peaks. Increasing P will decrease the array filling fraction and decrease the field coupling in nanopillars, which significantly weakens η_a peaks. However, the η_a peak distribution is broadened with decreased P due to increased interactions between pillars. Similar η_a dependences upon H and P also hold for the quadrupole mode.

In Fig. 3, we see that over 90% light absorption can be obtained from both dipole and quadrupole GaAs NPA resonators with properly optimized structures. The largest electron transportation efficiency, and potentially the strongest QE enhancement, can be achieved using the dipole mode due to its smaller pillar diameter, D. In this work, one GaAs NPA photocathode sample with a dipole resonance mode ($P = 600$ nm, $H = 350$ nm, $D = 120$ nm, labeled as $S1$) and two samples with quadrupole resonance modes ($P = 600$ nm, $H = 750$ nm, $D = 260$, and 280 nm, labeled as $S2$ and $S3$, respectively) within the wavelength range of 600–700 nm are fabricated. A SEM image of a fabricated GaAs NPA is shown in Fig. 4(a). Surface reflectance spectra for these three *NPA* samples together with a flat-wafer sample (labeled as $W1$) are shown in Fig. 4(b). It can be seen that the measured reflectance spectra and resonance peak wavelengths are in good agreement with calculations. Measurements indicate the reflectance of the flat wafer is greater than 35% across the entire visible spectral range, whereas the reflectance of all of the NPAs is only less than 6% at the resonance wavelengths.

B. Mie-resonance-enhanced photoelectron emission in GaAs NPA photocathode

The GaAs NPA and flat wafer samples are successfully activated to a NEA state. Measured QE spectra for all samples are presented in Fig. 5(a). Resonance modes can be seen in the QE spectra, and wavelength positions of QE maxima are in agreement with Mie resonance modes for corresponding geometries predicted from the computational model. This shows that across the entire visible

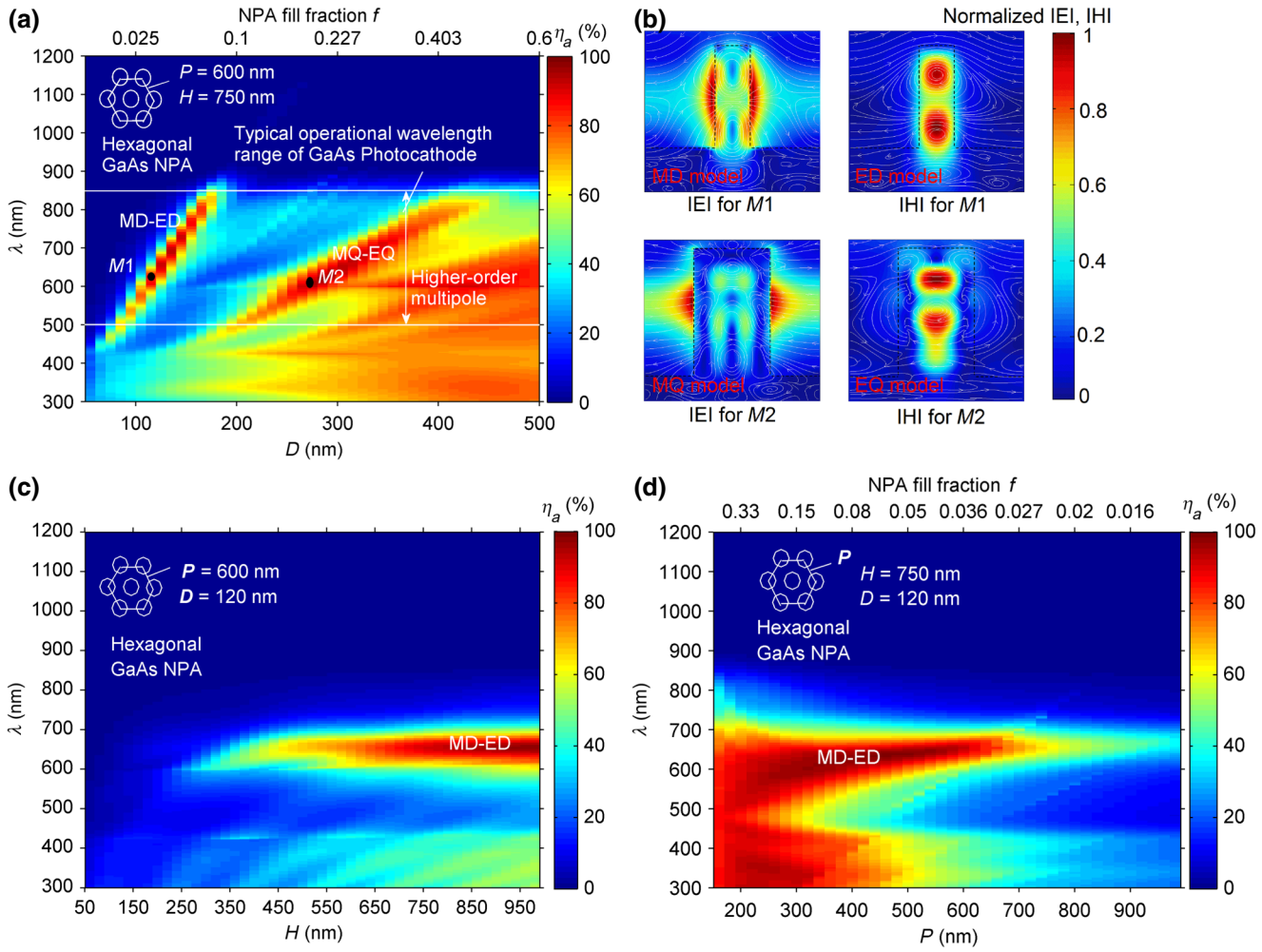

FIG. 3. Simulated light absorption spectra in GaAs NPA resonators. Absorption percentage indicated by color scale in all figures: (a) Dependence of η_a spectra upon diameter D when $P = 600$ nm and $H = 750$ nm. The black dots $M1$ ($D = 120$ nm) and $M2$ ($D = 260$ nm) correspond to wavelength and geometry combinations used in (b). (b) Normalized electric-magnetic field profiles (|E|-|H|, color) and field lines (white) in vertical crosscuts through the center of the nanopillars $M1$ (MD-ED resonance at 625 nm) and $M2$ (MQ-EQ resonance at 610 nm), respectively. (c) Dependence of η_a (color) spectra upon height H for dipole NPA resonator when $P = 600$ nm and $D = 120$ nm. (d) Dependence of η_a (color) spectra upon lattice period P for dipole NPA resonator when $D = 120$ nm and $H = 750$ nm.

spectrum, all of the NPAs have QE values greater than the flat wafer $W1$. At peak resonance wavelengths ($\lambda = 620$ nm for $S1$, 627 nm for $S2$, and 655 nm for $S3$), the NPA samples exhibit QE enhancement by factors of 1.8, 3.5, and 3, respectively, compared with that of flat wafer $W1$.

It should be noted that all of the photocathode samples described in this report are directly exposed to air for several months before testing and are not chemically cleaned before installation inside the ultrahigh vacuum chamber. Impurities and defects can be introduced onto the surface during air exposure, sample handling, vacuum chamber bake out, and during the NPA etching processes, which will increase the electron recombination rate, adversely impact the qualities of NEA surface condition, and lead to lower QE [9,15,16,36,37]. To gauge this impact, NPA photocathode QE results are also compared to the best QE results of a previously tested "epiready" GaAs flat wafer [15] labeled as $W2$ and shown as a green line in Fig. 4(a), which also underwent the same QE measurement processes using the same vacuum apparatus. It can be seen that flat wafer $W1$ suffers more surface contamination compared to flat wafer $W2$, providing only half the QE. But even when comparing the NPA results to sample $W2$, QE enhancement factors of 1.5 and 1.3 at the resonance peaks are still achieved from $S2$ and $S3$, respectively.

The QE stability (also referred to as QE photocurrent lifetime) of the NEA state for GaAs NPA sample $S2$ is also measured [Fig. 5(b)]. When illuminated with a 15-μW light at 630 nm, the QE of sample $S2$ decreases by 50% after 40 h of continuous photoemission at current >1 μA. This

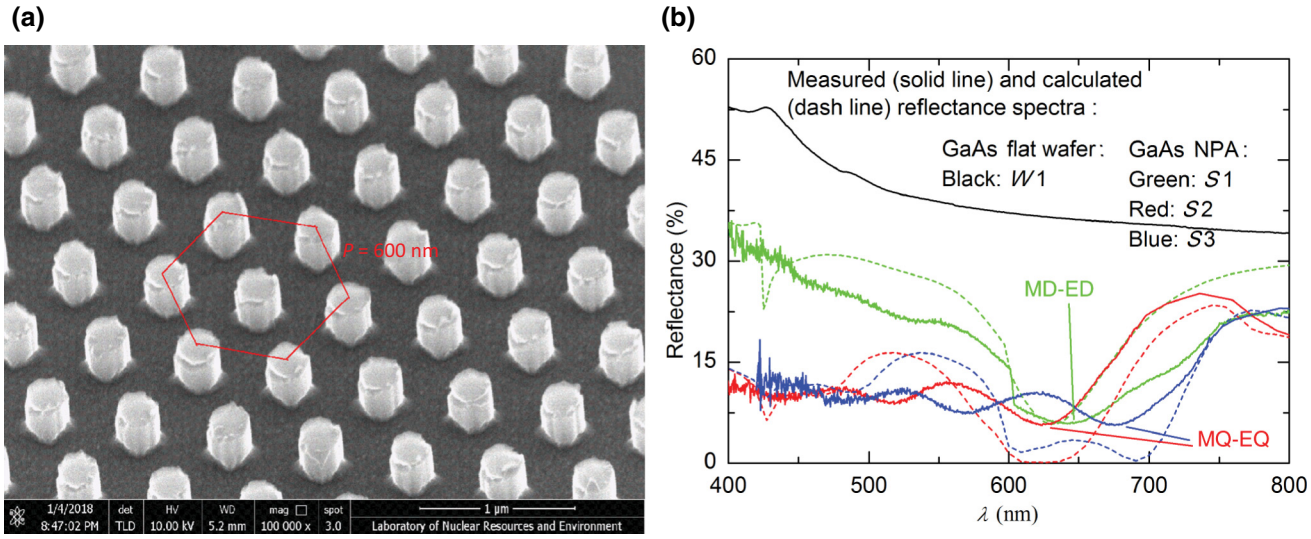

FIG. 4. Surface morphology and reflectance spectra of GaAs NPA fabricated by SCIL on GaAs substrate. (a) SEM image of the NPA on GaAs substrate. (b) Measured (solid line) and calculated (dash line) reflectances of GaAs NPA samples $S1$ ($D = 120$ nm, $H = 350$ nm, $P = 600$ nm), $S2$ ($D = 260$ nm, $H = 750$ nm, $P = 600$ nm), and $S3$ ($D = 280$ nm, $H = 750$ nm, $P = 600$ nm). The reflectance of a GaAs flat wafer $W1$ is also measured and shown in (b).

result is quite good compared to measurements performed with similar vacuum chambers. The QE stability of a GaAs photocathode is largely dependent on the vacuum conditions under which the measurement occurs. Practical high-voltage photoguns used at modern accelerators [5–8] can be expected to provide better vacuum, and therefore, better stability than reported here. The excellent NEA activation performance of NPA photocathodes can be also attributed to the larger effective active surface area compared to that of a flat wafer. It is also expected that even higher QE and better NEA stability can be achieved by optimizing the fabrication and surface cleaning processes.

The GaAs NPA photocathode performances are analyzed by fitting the two-valley diffusion model as mentioned in Sec. II to the measured QE. Figures 6(a) and 6(b) show the theoretical and measured QE spectra for the geometries of samples $S1$ and $S2$, respectively. The QE contributions from the NPA and the substrate

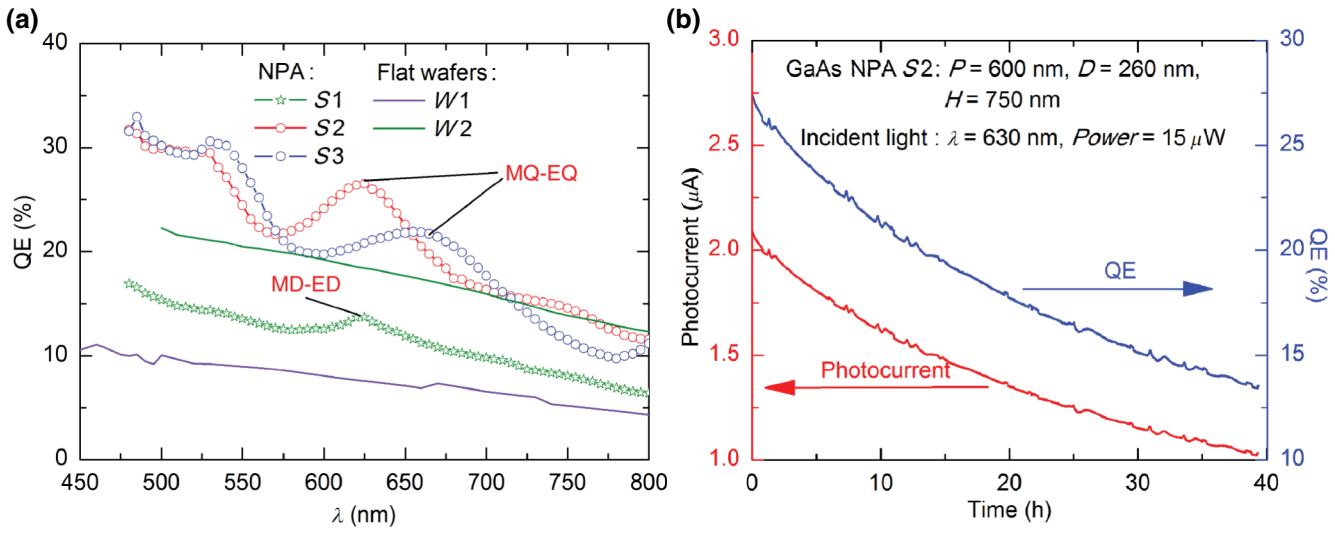

FIG. 5. Photoemission performances of the GaAs NPA and flat wafer photocathodes. (a) Measured QE spectra of the GaAs NPA samples $S1$ ($D = 120$ nm, $H = 350$ nm, $P = 600$ nm), $S2$ ($D = 260$ nm, $H = 750$ nm, $P = 600$ nm), $S3$ ($D = 280$ nm, $H = 750$ nm, $P = 600$ nm), and GaAs flat wafer samples $W1$ (flat wafer exposed to air in this work), $W2$ (epiready flat wafer reported previously [15]). (b) Dependence of photocurrent and QE on operational time for GaAs NPA sample $S2$ under the incident light wavelength of 630 nm and power of 15 μW.

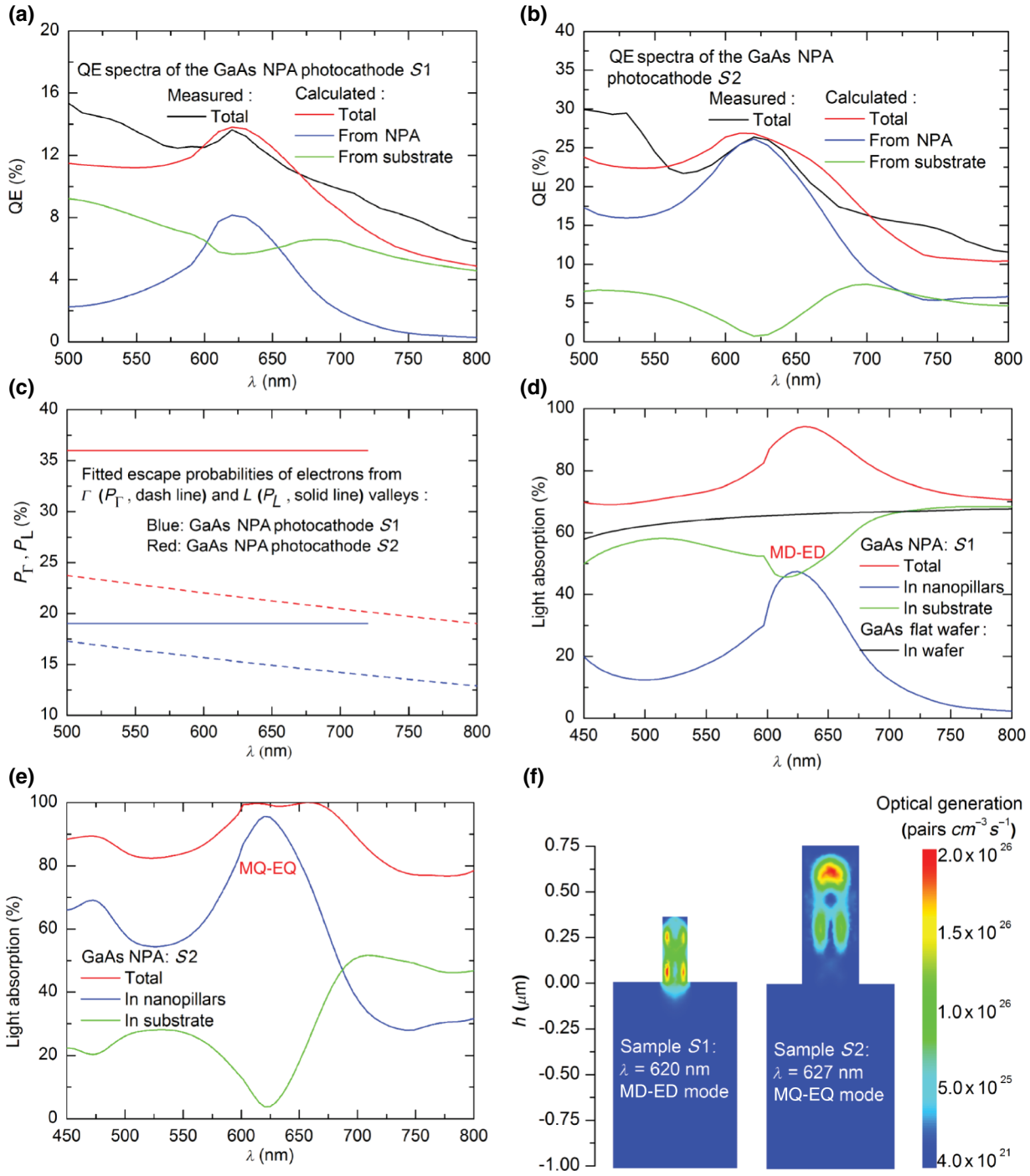

FIG. 6. Analysis of the GaAs NPA photocathodes $S1$ and $S2$ by fitting the two-valleys model to the measured QE. (a) and (b) are the QE spectra of the samples $S1$ and $S2$. (c) The fitted escape probabilities of electrons emitted into vacuum from the Γ (P_Γ) and L (P_L) valleys. (d) and (e) are the calculated light absorption in GaAs NPA $S1$ and $S2$ and the flat wafer. (f) Distribution of photoelectron generation rate in (pairs $\mathrm{cm}^{-3}\ \mathrm{s}^{-1}$) within the vertical cross sections of the samples $S1$ and $S2$ in the plane parallel to the E field of the linearly polarized incident light (light intensity is $1\ \mathrm{W\,cm}^{-2}$) at the resonance wavelength.

are calculated separately and illustrate the significant QE enhancement from NPA at the resonance wavelengths. The sum of the two calculated components agrees reasonably well with the measured QE, especially for the Mie-resonance-wavelength range within 600–700 nm. The significant deviations occur at the short wavelength end for both of the two samples, possibly due to the omission of the photoemission from the higher X valley at the

higher incident photon energy in the two-valley model. Figure 6(c) shows the fitted escape probabilities of electrons emitted into vacuum from the Γ (P_Γ) and L (P_L) valleys. For the electrons in the L valley with the high energy level, constant P_L is selected for $\lambda < 725$ nm (cutoff wavelength of the incident photons that excite the electrons from the valence band to the L valley of the conduction band for GaAs) due to little impact from the surface barrier. For the electrons in the Γ valley, however, the impact from the surface barrier should be considered and P_Γ is decreased with the incident photon energy as shown in Fig. 6(c).

Light absorption is calculated using FDTD simulations for GaAs NPA photocathodes $S1$ and $S2$ as shown in Figs. 6(d) and 6(e), respectively. For the resonance wavelength range within 600–700 nm, light absorption of larger than 90% that is mainly contributed by nanopillars is obtained in $S1$ and $S2$, compared to approximately 65% in the flat wafer, which is one of the factors for the QE enhancement by NPA. Figure 6(f) shows the generation rates are concentrated in the nanopillars, especially for the $S2$ with a larger pillar height. Light absorption in the nanopillars of $S1$ and $S2$ at the resonance wavelengths is enhanced by a factor of 25 and 9, respectively, with respect to the equivalent flat wafer. These highly localized photoelectrons in nanopillars can be transported to the top and side surfaces more efficiently due to the much lower travel distance then that of the flat wafer, which constitutes another important factor for the QE enhancement.

As a final assessment of the GaAs NPA photocathode, the related performances at the resonance wavelengths for the investigated NEA photocathodes are listed in Table I. The emission area enhancement factors, r_{emi}, defined by Eq. (1) are also calculated and listed in Table I. The photoelectron emission QE contributions from the Γ (QE_Γ) and L (QE_L) valleys are calculated separately and illustrate significant enhancement from the L valley of the nanopillar due to its much lower electron travel distance than that of the flat wafer. For the NPA sample $S2$, all of the photoelectron emission performance parameters in Table I are larger than that for the flat wafer $W1$, which leads to a QE enhancement by a factor of 3.5. Whereas for NPA sample $S1$, the smaller pillar height leads to a larger portion of the incident light being coupled into the substrate. Since more light is absorbed, but not as many electrons are emitted, the QE enhancement is only a factor of 1.3. The fitted escape probabilities of electrons, P_Γ and P_L, of $S1$ are also lower than that of $S2$, which indicates the poorer surface NEA activation quality of $S1$. It also shows in Table I that a total light absorption of over 90% can be achieved for NPA photocathodes and the escape probability of electrons below 36% is the main limiting factor for the QE enhancement. Therefore, we believe further QE enhancement may be achieved with an improved surface NEA state by improving the NPA fabrication and NEA activation processes in the future.

IV. CONCLUSIONS

In conclusion, we present evidence that a rational design of photocathodes using materials with a high index of refraction formed into resonant nanostructures can provide superior performances for photocathodes and other high-brightness electron emission sources. We demonstrate excitation of Mie-type resonances in GaAs NPA that result in significant QE enhancement. High QE is extremely important for dc high-voltage photogun applications, particularly for accelerator applications that demand very high beam currents with long operational lifetimes. We suggest that such structures can simultaneously provide a nonreflective surface ("dark" over visible wavelengths) that can be tuned for optimal responses in specific wavelength ranges where high-power, linearly polarized, time-tunable laser sources are readily available. Such optically dark photocathode surfaces minimize scattered light within the photogun, avoiding unwanted photoemission from the edge of the photocathode that can lead to electron leakage that strikes the vacuum chamber walls degrading the vacuum, lowering QE, and reducing photocathode lifetime via ion back bombardment [15,22]. The results reported here, namely <27% QE and >90% light absorption, demonstrate the feasibility of this approach. We discuss the need for further work to optimize the fabrication processes and thereby to reduce damage or contamination during etching, handling, activation, and vacuum practice during operation. These steps will lead to further

TABLE I. Photoemission performances of GaAs NPA and flat wafer photocathodes at the resonance wavelengths (λ_r).

Samples	Resonance model and wavelength λ_r	Materials	Light absorption	Fitted P_Γ	Fitted P_L	r_{emi}	Modeled QE_Γ	Modeled QE_L	Measured QE
NPA: $S1$	MD-ED model	nanopillar	47.25%	15.36%	19.00%	1.42	2.83%	5.32%	13.64%
	$\lambda_r = 620$ nm	substrate	45.83%	15.36%	19.00%		4.65%	1.00%	
NPA: $S2$	MQ-EQ model	nanopillar	95.36%	21.56%	36.00%	3.12	10.85%	14.42%	26.58%
	$\lambda_r = 627$ nm	substrate	3.85%	21.56%	36.00%		0.73%	0.19%	
wafer: $W1$	No resonance	wafer	65.78%	15.36%	17.00%	1.00	6.67%	1.28%	7.63%
	$\lambda = 620$ nm								

improvement of QE and to longer life for NEA cathodes. It seems reasonable that nanostructured Mie-type resonators can be extended to other materials, in particular the strained superlattice GaAs-based photocathodes to provide high QE and higher spin polarization. In the future, these nanophotonic photocathodes must be tested inside a photogun operating at high bias voltage to determine if the nanostructured device poses field emission problems, and to measure beam emittance and photocathode lifetime, which are important metrics for photogun operation under a practical accelerator environment.

ACKNOWLEDGMENTS

The authors would like to thank Olga Trofimova and Benjamin Kincaid for assistance with the SEM characterizations. This work was partially supported by the National Natural Science Foundation of China (Grants No. 11875012, No. 61204071, and No. 61661002) and authored by Jefferson Science Associates, LLC under U.S. DOE Contract No. DE-AC05-06OR23177. The U.S. Government retains a nonexclusive, paid-up, irrevocable, worldwide license to publish or reproduce this manuscript for U.S. Government purposes.

[1] A. I. Kuznetsov, A. E. Miroshnichenko, M. L. Brongersma, Y. S. Kivshar, and B. Luk'yanchuk, Optically resonant dielectric nanostructures, Science **354**, aag2472 (2016).

[2] M. T. Sheldon, J. Groep, A. M. Brown, A. Polman, and H. A. Atwater, Plasmoelectric potentials in metal nanostructures, Science **346**, 828 (2014).

[3] S. Jahani and Z. Jacob, All-dielectric metamaterials, Nat. Nanotechnol. **11**, 23 (2016).

[4] X. Jin, S. Ohki, T. Ishikawa, A. Tackeuchi, and Y. Honda, Analysis of quantum efficiency improvement in spin-polarized photocathode, J. Appl. Phys. **120**, 164501 (2016).

[5] S. Karkare, L. Boulet, L. Cultrera, B. Dunham, X. Liu, W. Schaff, and I. Bazarov, Ultrabright and Ultrafast III–V Semiconductor Photocathodes, Phys. Rev. Lett. **112**, 097601 (2014).

[6] D. Abbott *et al.*, Production of Highly Polarized Positrons Using Polarized Electrons at MeV Energies, Phys. Rev. Lett. **116**, 214801 (2016).

[7] N. A. Moody, K. L. Jensen, A. Shabaev, S. G. Lambrakos, J. Smedley, D. Finkenstadt, J. M. Pietryga, P. M. Anisimov, V. Pavlenko, E. R. Batista, J. W. Lewellen, F. Liu, G. Gupta, A. Mohite, H. Yamaguchi, M. A. Hoffbauer, and I. Robel, Perspectives on Designer Photocathodes for X-ray Free-Electron Lasers: Influencing Emission Properties with Heterostructures and Nanoengineered Electronic States, Phys. Rev. Appl. **10**, 047002 (2018).

[8] D. Wu *et al.*, First lasing of the CAEP THz FEL facility driven by a superconducting accelerator, J. Phys. Conf. Ser. **1067**, 032010 (2018).

[9] Y. Zhang, Y. Qian, C. Feng, F. Shi, H. Cheng, J. Zou, J. Zhang, and X. Zhang, Improved activation technique for preparing high-efficiency GaAs photocathodes, Opt. Mater. Express **7**, 3456 (2017).

[10] G. Tang, F. Yan, X. Chen, and W. Luo, High-quantum-efficiency ultraviolet solar-blind AlGaN photocathode detector with a sharp spectral sensitivity threshold at 300 nm, Appl. Opt. **57**, 8060 (2018).

[11] B. Liao and E. Najafi, Scanning ultrafast electron microscopy: A novel technique to probe photocarrier dynamics with high spatial and temporal resolutions, Mater. Today Phys. **2**, 46 (2017).

[12] J. E. Schneider, P. Sen, D. S. Pickard, G. I. Winograd, M. A. McCord, R. F. W. Pease, W. E. Spicer, A. W. Baum, K. A. Costello, and G. A. Davis, Patterned negative electron affinity photocathodes for maskless electron beam lithography, J. Vac. Sci. Technol. B **16**, 3192 (1998).

[13] X. Jin, B. Ozdol, M. Yamamoto, A. Mano, N. Yamamoto, and Y. Takeda, Effect of crystal quality on performance of spin-polarized photocathode, Appl. Phys. Lett. **105**, 203509 (2014).

[14] C. Hernandez-Garcia, M. Poelker, and J. Hansknecht, High voltage studies of inverted-geometry ceramic insulators for a 350 kV DC polarized electron gun, IEEE T. Dielect. El. In **23**, 418 (2016).

[15] W. Liu, S. Zhang, M. L. Stutzman, and M. Poelker, The effects of ion bombardment on bulk GaAs photocathodes with different surface- cleavage planes, Phys. Rev. Accel. Beams **19**, 103402 (2016).

[16] S. Zhang, S. V. Benson, and C. H-Garcia, Observation and measurement of temperature rise and distribution on GaAs photo-cathode wafer with a 532 nm drive laser and a thermal imaging camera, Nucl. Instrum. Methods A **631**, 22 (2011).

[17] J. Zou, W. Zhao, X. Ding, Z. Zhu, W. Deng, and W. Wang, Spectral sensitivity of graded composition AlGaAs/GaAs nanowire photodetectors, Appl. Phys. A **122**, 1003 (2016).

[18] W. Deng, J. Zou, X. Peng, L. Feng, Z. Zhu, W. Wang, Y. Zhang, and B. Chang, Resolution characteristics of graded doping and graded composition transmission-mode AlGaAs/GaAs photocathodes, Appl. Opt. **54**, 1414 (2015).

[19] W. Liu, Y. Chen, W. Lu, A. Moy, M. Poelker, M. Stutzman, and S. Zhang, Record-level quantum efficiency from a high polarization strained GaAs/GaAsP superlattice photocathode with distributed Bragg reflector, Appl. Phys. Lett. **109**, 252104 (2016).

[20] J. K. Bae, L. Cultrera, P. DiGiacomo, and I. Bazarov, Rugged spin-polarized electron sources based on negative electron affinity GaAs photocathode with robust Cs2Te coating, Appl. Phys. Lett. **112**, 154101 (2018).

[21] J. Zou, X. Ge, Y. Zhang, W. Deng, Z. Zhu, W. Wang, X. Peng, Z. Chen, and B. Chang, Negative electron affinity GaAs wire-array photocathodes, Opt. Express **24**, 4632 (2016).

[22] J. Grames, R. Suleiman, P. A. Adderley, J. Clark, J. Hansknecht, D. Machie, M. Poelker, and M. L. Stutzman, Charge and fluence lifetime measurements of a DC high voltage GaAs photogun at high average current, Phys. Rev. ST Accel. Beams **14**, 043501 (2011).

[23] A. F. Cihan, A. G. Curto, S. Raza, P. G. Kik, and M. L. Brongersma, Silicon mie resonators for highly directional

light emission from monolayer MoS2, Nat. Photon. **12**, 284 (2018).
[24] L. Cao, P. Fan, A. P. Vasudev, J. S. White, Z. Yu, W. Cai, J. A. Schuller, S. Fan, and M. L. Brongersma, Semiconductor nanowire optical antenna solar absorbers, Nano Lett. **10**, 439 (2010).
[25] J. Groep and A. P. Center, Designing dielectric resonators on substrates: Combining magnetic and electric resonances, Opt. Express **21**, 26285 (2013).
[26] L. Wen, Z. Zhao, X. Li, Y. Shen, H. Guo, and Y. Wang, Theoretical analysis and modeling of light trapping in high efficiency GaAs nanowire array solar cells, Appl. Phys. Lett. **99**, 143116 (2011).
[27] P. Krogstrup, H. I. Jørgensen, M. Heiss, O. Demichel, J. V. Holm, M. Aagesen, J. Nygard, and A. F. Morral, Single-nanowire solar cells beyond the Shockley-Queisser limit, Nat. Photon. **7**, 306 (2013).
[28] Y. Yang, X. Peng, S. Hyatt, and D. Yu, Broadband quantum efficiency enhancement in high index nanowire resonators, Nano Lett. **15**, 3541 (2015).
[29] Z. Geng, X. Guo, Q. Kan, and H. Chen, Optimization of substrate conformal imprint lithography (SCIL) and etching for nanostructure, AIP Adv. **5**, 041308 (2015).
[30] W. E. Spicer, Negative affinity 3–5 photocathodes: Their physics and technology, Appl. Phys. A **12**, 115 (1977).
[31] J. Zou, Y. Zhang, X. Peng, W. Deng, L. Feng, and B. Chang, Energy distributions of electrons emitted from reflection-mode Cs-covered GaAs photocathodes, Appl. Optics **51**, 7662 (2012).
[32] J. Zou, B. Chang, H. Chen, and L. Liu, Variation of quantum-yield curves for GaAs photocathodes under illumination, J. Appl. Phys. **101**, 033126 (2007).
[33] J. Zou, B. Chang, Z. Yang, Y. Zhang, and J. Qiao, Evolution of surface potential barrier for negative-electron-affinity GaAs photocathodes, J. Appl. Phys. **105**, 013714 (2009).
[34] FDTD Solutions, Lumerical Solutions, Inc., http://www.lumerical.com.
[35] VisualTCAD 1.9.3, Cogenda Pte Ltd, http://www.cogenda.com/.
[36] Y. Sun, R. E. Kirby, T. Maruyama, G. A. Mulhollan, J. C. Bierman, and P. Pianetta, The surface activation layer of GaAs negative electron affinity photocathode activated by Cs, Li and NF3, Appl. Phys. Lett. **95**, 174109 (2009).
[37] L. Guo, M. Kuriki, H. Iijima, and K. Uchida, NEA surface activation of GaAs photocathode with different gases, Surf. Sci. **664**, 65 (2017).